SHORT REPORT

3D electron tomography of brain tissue unveils distinct Golgi structures that sequester cytoplasmic contents in neurons

Maria Rosario Fernandez-Fernandez*, Desire Ruiz-Garcia, Eva Martin-Solana, Francisco Javier Chichon, Jose L. Carrascosa and Jose-Jesus Fernandez*

ABSTRACT

Macroautophagy is morphologically characterized by autophagosome formation. Autophagosomes are double-membraned vesicles that sequester cytoplasmic components for further degradation in the lysosome. Basal autophagy is paramount for intracellular quality control in post-mitotic cells but, surprisingly, the number of autophagosomes in post-mitotic neurons is very low, suggesting that alternative degradative structures could exist in neurons. To explore this possibility, we have examined neuronal subcellular architecture by performing three-dimensional (3D) electron tomography analysis of mouse brain tissue that had been preserved through high-pressure freezing. Here, we report that sequestration of neuronal cytoplasmic contents occurs at the Golgi complex in distinct and dynamic structures that coexist with autophagosomes in the brain. These structures are composed of several concentric double-membraned layers that appear to be formed simultaneously by the direct bending and sealing of discrete Golgi stacks. These structures are labelled for proteolytic enzymes, and lysosomes and late endosomes are found in contact with them, leading to the possibility that the sequestered material could be degraded inside them. Our findings highlight the key role that 3D electron tomography, together with tissue rapid-freezing techniques, will have in gaining new knowledge about subcellular architecture.

KEY WORDS: Golgi complex, Brain tissue, Neuron, High-pressure freezing, Electron tomography

INTRODUCTION

Macroautophagy is a cellular process that is involved in protein and organelle degradation with diverse physiological implications. It is morphologically characterized by the formation of double-membraned vesicles termed autophagosomes (Cuervo and Macian, 2012; Mizushima et al., 2008). The deletion of genes coding for essential proteins in autophagosome formation causes neurodegeneration (Hara et al., 2006; Komatsu et al., 2006), revealing that the degradation of cytoplasmic contents is crucial for basal neuronal homeostasis. Surprisingly, the number of autophagosomes is very low in neurons (Mizushima et al., 2004; Nixon et al., 2005), which can be partly explained by the rapid clearance of autophagosomes in healthy neurons (Boland et al., 2008). Alternatively, pathways and/or structures that have not yet

been identified might cooperate with neuronal autophagosomes in the degradation of cytoplasmic content. The Golgi complex has previously been identified as a membrane donor for conventional autophagosome formation both in yeast and mammalian systems (Ohashi and Munro, 2010; van der Vaart and Reggiori, 2010; Young et al., 2006).

For conventional electron microscopy, dehydrated specimens are prepared by chemical fixation, which is known to induce artefacts, to be inadequate for capturing dynamic events and to be particularly unsuitable for the preservation of membrane-rich structures (He and Fernandez, 2010; Korogod et al., 2015). Nowadays, optimal structural preservation can be achieved by preparing the specimens with rapid-freezing techniques. In particular, high-pressure freezing (HPF) can fully vitrify a bulk specimen (up to 200–400 μm) by means of delivering synchronized pressurization and cooling of the sample within milliseconds. Freeze-substitution involves the slow replacement of frozen cellular water with organic solvents at low temperature (−90°C range). At this temperature, large molecules and organelles are immobile but small molecules and solvents can penetrate cells (He and Fernandez, 2010). The combination of HPF and freeze-substitution techniques is actually the most adequate combination for the ultrastructural analysis of brain samples with high-resolution imaging (Korogod et al., 2015; Studer et al., 2014). Electron tomography is based on the acquisition of images from the specimen at different tilt angles, which are subsequently processed and combined to yield a three-dimensional (3D) reconstruction, or tomogram (Fernandez, 2012). The combination of HPF with freeze-substitution and electron tomography has been previously employed to analyze synaptic ultrastructure in brain tissue (Rostaing et al., 2006; Siksou et al., 2009).

We have set up a protocol to preserve mouse brain striatal tissue by using HPF and freeze-substitution. Use of electron tomography to analyze these samples has made it possible to identify and characterize distinct Golgi structures that coexist with neuronal autophagosomes and that might cooperate in the degradation of cytoplasmic contents.

RESULTS AND DISCUSSION

Identification of distinct Golgi structures in cryopreserved brain tissue

Mouse striatal tissue was subjected to HPF and freeze-substitution. The high-quality preservation of the tissue was confirmed by performing transmission electron microscopy analysis (Fig. 1A). The tissue showed a uniform appearance with well-contrasted cell bodies and neuropil. At higher magnification, we identified specific Golgi structures composed of several concentric double-membraned layers (Fig. 1B–E). These Golgi structures engulfed cytoplasmic contents and were found to be at different stages of closure; they appeared as cup-shaped (Fig. 1B,E) or as completely closed structures (Fig. 1C,D). These engulfing structures were
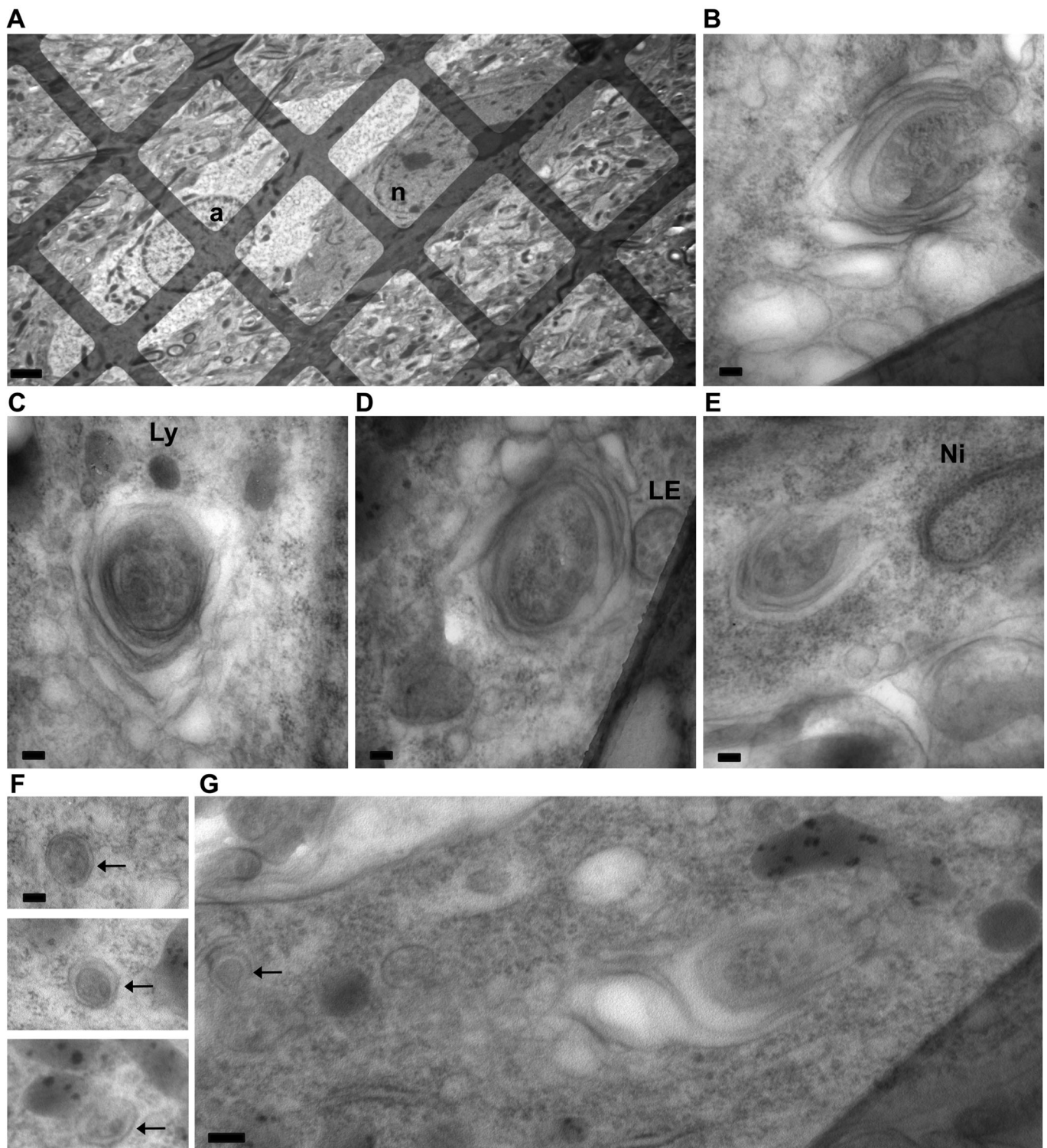
Fig. 1. Identification of distinct Golgi structures in mouse striatal tissue preserved through HPF and freeze-substitution. (A) Observation of 250-nm sections at low magnification confirmed high-quality preservation of tissue. (B–E) Golgi structures at different stages of closure are found in neurons. The Golgi origin is evidenced by comparison with endoplasmic reticulum membranes (Nissl body in E). (F) Neuronal autophagosomes. (G) Engulfing Golgi and autophagosomes coexist in neuronal soma. Arrows point to autophagosomes. a, astrocyte; LE, late endosome; Ly, lysosome; n, neuron; Ni, Nissl body. Images are from a 9-month-old male mouse. Scale bars: 2 μm (A); 100 nm (B–F); 200 nm (G).

larger than nearby autophagosomes (Fig. 1F) and they coexisted in the neuronal soma (Fig. 1G). The electron microscopy images shown in this paper correspond to samples from 9-month-old animals. We also identified these engulfing structures at 2 and 6 months of age (data not shown) with no apparent difference across the ages (quantifications are shown in Table S1). The structures were also detected in samples that had been processed using conventional electron microscopy fixation methods (Fig. S1A).
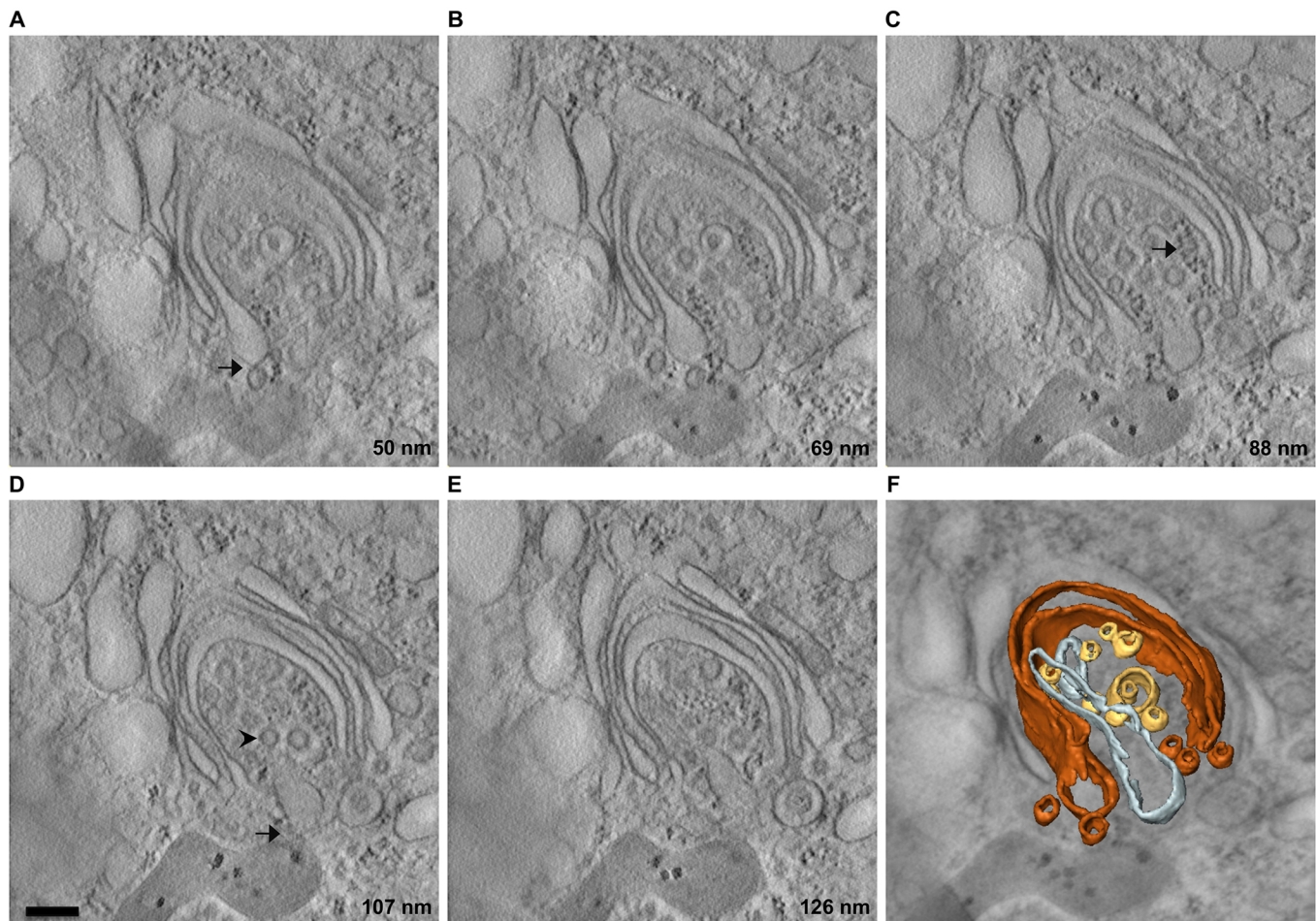
Fig. 2. Visualization of the 3D architecture of an engulfing Golgi in the open state. (A–E) Representative 3.12-nm-thick slices from the 3D volume at an interval of 19 nm. The position of the slice relative to the bottom edge of the volume is indicated at the bottom right corner. This tomogram corresponds to the structure shown in Fig. 1B. The eventual closure of the isolation structure appears to be mediated by the fusion of Golgi-derived vesicles to the rims of the cisternae as indicated in A (arrow). Different cytoplasmic contents are in the process of being engulfed: ribosome-rich structures (Nissl bodies, arrow in C), Golgi-derived vesicles (arrowhead in D) or a cytoplasmic structure connected to a mitochondrion (arrow in D). (F) 3D model visualized on a background showing the projection of the whole structure. For simplicity, only selected structures are shown in 3D. The cisterna that is closer to the engulfed material is highlighted in orange for a better visualization of its cup-shaped structure. Golgi-derived vesicles that could be contributing to the closure of the isolation cisterna are also shown in orange. Additional Golgi-derived vesicles are shown in yellow. Other cytoplasmic structures are shown in grey. Movie 1 shows a detailed view of the slices of the tomogram and the 3D model. Scale bar: 200 nm.

Engulfing structures coexisted with classic Golgi stacks in samples that had been preserved by using HPF (Fig. S1B).

3D characterization of engulfing Golgi by using electron tomography

We next performed electron tomography to visualize the 3D architecture of engulfing Golgi. Computational slices across the 3D volumes highlight the details of representatives of the open (Fig. 2; Fig. S2) and closed structures (Fig. 3; Fig. S2). Formation of these structures involves the simultaneous bending of several Golgi cisternae to form a cup-shaped isolation structure made up of several concentric layers of double membrane (Fig. 2; Fig. S2 and Movie 1). Although the precise mechanism of their formation still remains to be established, the presence of Golgi-derived vesicles in the vicinity of cisternal rims leads us to speculate that the elongation and sealing of the isolation structures is made possible by the fusion of these vesicles to the rims of each individual cisterna (Fig. 2A, arrow). These structures engulf different cytoplasmic components that are clearly identifiable (e.g. vesicles, Nissl bodies) (Fig. 2). In the closed state, the engulfed cytoplasmic material is completely isolated by concentric double-membraned layers (Fig. 3; Figs S2, S3 and Movie 2).

The appearance of the vesicles that could contribute to the sealing (thick membranes) (Fig. 2A) suggests that the trans-most cisternae are the direct isolation membranes. In accordance with this notion, immunolabelling for TGN38 (also known as TGOLN2; a marker for the trans-Golgi network and trans-most cisternae) and giantin (also known as GOLGB1; cis-mid Golgi marker) revealed these two proteins were preferentially associated with the inner and outer layers, respectively (Fig. 4A). Confocal microscopy analysis of immunolabelling of TGN38 identified discrete perinuclear structures with dimensions that were compatible with the central area of the engulfing structures. Consequently, staining for giantin labelled similar structures with larger diameters and non-labelled central areas. Double labelling for TGN38 and GM130 (also known as GOLGA2; a cis-Golgi marker) corroborated that the central part of these structures was derived from the trans-Golgi (Fig. 4B). A schematic representation of the model proposed for the formation of these Golgi structures is depicted in Fig. 4C.
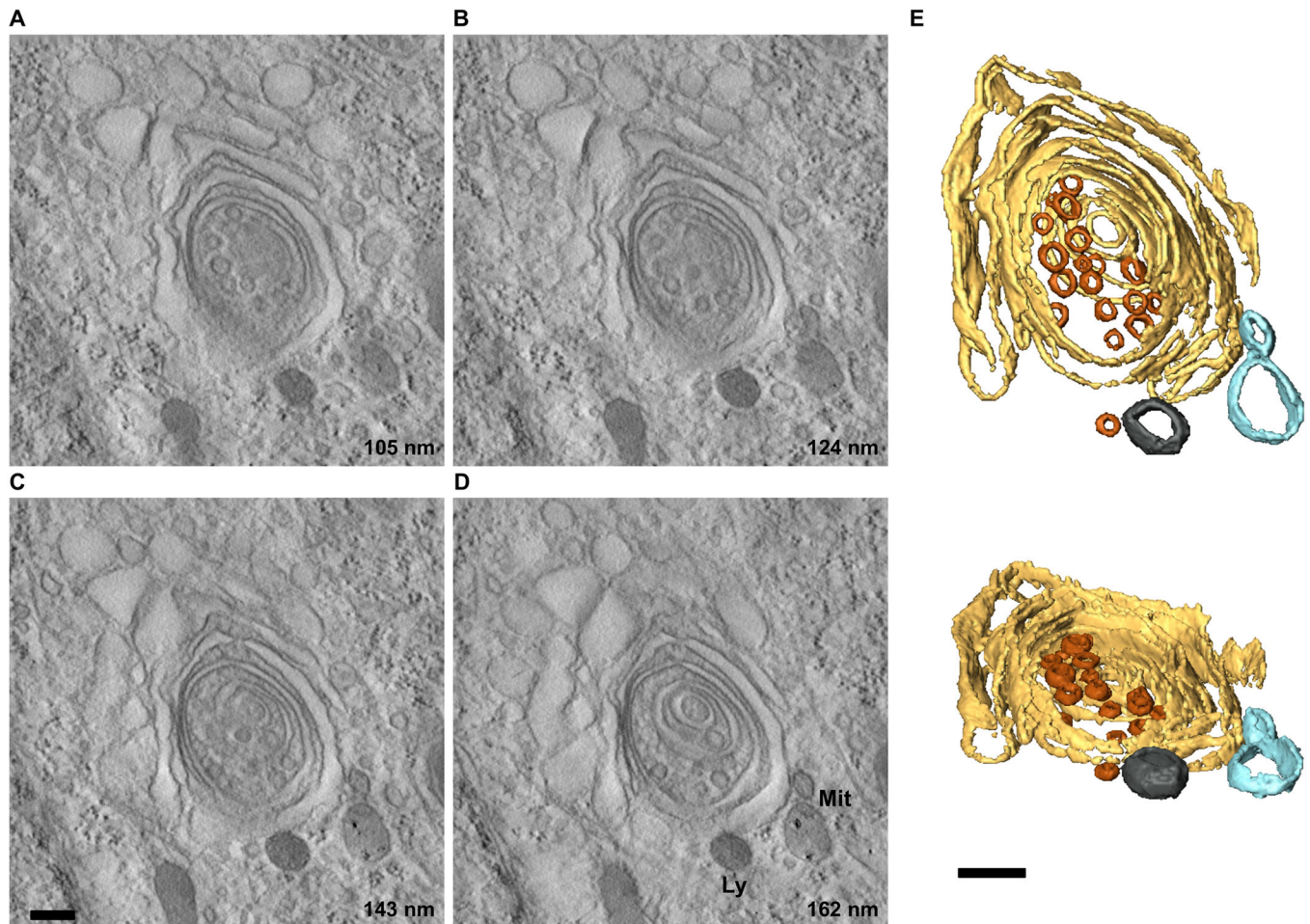
Fig. 3. Visualization of the 3D architecture of an engulfing Golgi in the closed state. (A–D) Representative 3.76-nm-thick slices from the 3D volume at an interval of 19 nm. The position of the slice relative to the bottom edge of the volume is indicated at the bottom right corner. This corresponds to the structure shown in Fig. 1C. Ly, lysosome; Mit, mitochondrion. (E) 3D views of the model with segmented membranes. Golgi stack in yellow, vesicles in orange, mitochondrion in cyan and lysosome in black. Movie 2 shows a detailed view of the slices of the tomogram and the 3D model. Scale bars: 200 nm.

The engulfing Golgi is a potential site for degradation of cytoplasmic contents

Proteolytic enzymes are commonly provided to autophagosomes through fusion with late endosomes or lysosomes (Mizushima et al., 2008; Nixon et al., 2005). Both of these organelles are recognizable in the proximity of or in close contact with the engulfing Golgi (Fig. 1C,D and Fig. 3). Confocal microscopy analysis confirmed that the discrete structures that were labelled for giantin and TGN38 were found close to LAMP1 labelling (lysosomal marker) (Fig. 4B). The immunolabelling for cathepsin B (a typical lysosomal protease) revealed the presence of the protease in the structures (Fig. 4D). Moreover, confocal images confirmed that the labelling for cathepsin B was found to be enriched in the proximity of Golgi markers (Fig. 4D). Thus, degradative enzymes could be provided in the absence of a complete fusion between the Golgi structures and lysosomes through a kiss-and-run mechanism that is similar to that proposed for material transfer between endosomes and lysosomes (Luzio et al., 2007). It is well established that degradative enzymes are delivered to lysosomes through the Golgi complex (Kornfeld and Mellman, 1989; Traub and Kornfeld, 1997); therefore, it is also possible that enzymes that have not yet exited the Golgi complex could somehow accomplish their degradative function through an unconventional mechanism. The presence of engulfed cytoplasmic material was confirmed by the presence of COX IV labelling (a mitochondrial inner membrane protein) inside them (Fig. 4E). We confirmed that the number of conventional autophagosomes was low in striatal neurons by observing the diffuse cytoplasmic pattern of LC3 (the most widely monitored autophagosomal protein; MAP1LC3B isoform) in confocal images and the small ratio of lipidated to non-lipidated LC3 detected by western blotting (Fig. S1C). These results suggest that these Golgi structures might act as degradative intermediates, but further work is required to definitively establish this notion.

The identification and characterization of the engulfing Golgi would have been difficult by using conventional molecular and cell biology methods, thereby reinforcing the power of new 3D imaging technologies and optimal preservation of samples to address fundamental questions in cell physiology and architecture. Moreover, our findings have provided knowledge about the complexity and diversity of neuronal homeostasis. The fact that post-mitotic neurons need to adapt rapidly to changing conditions supports the implication of the Golgi complex, a dynamic organelle, in the degradation of cytoplasmic contents through the formation of the described engulfing Golgi structures.
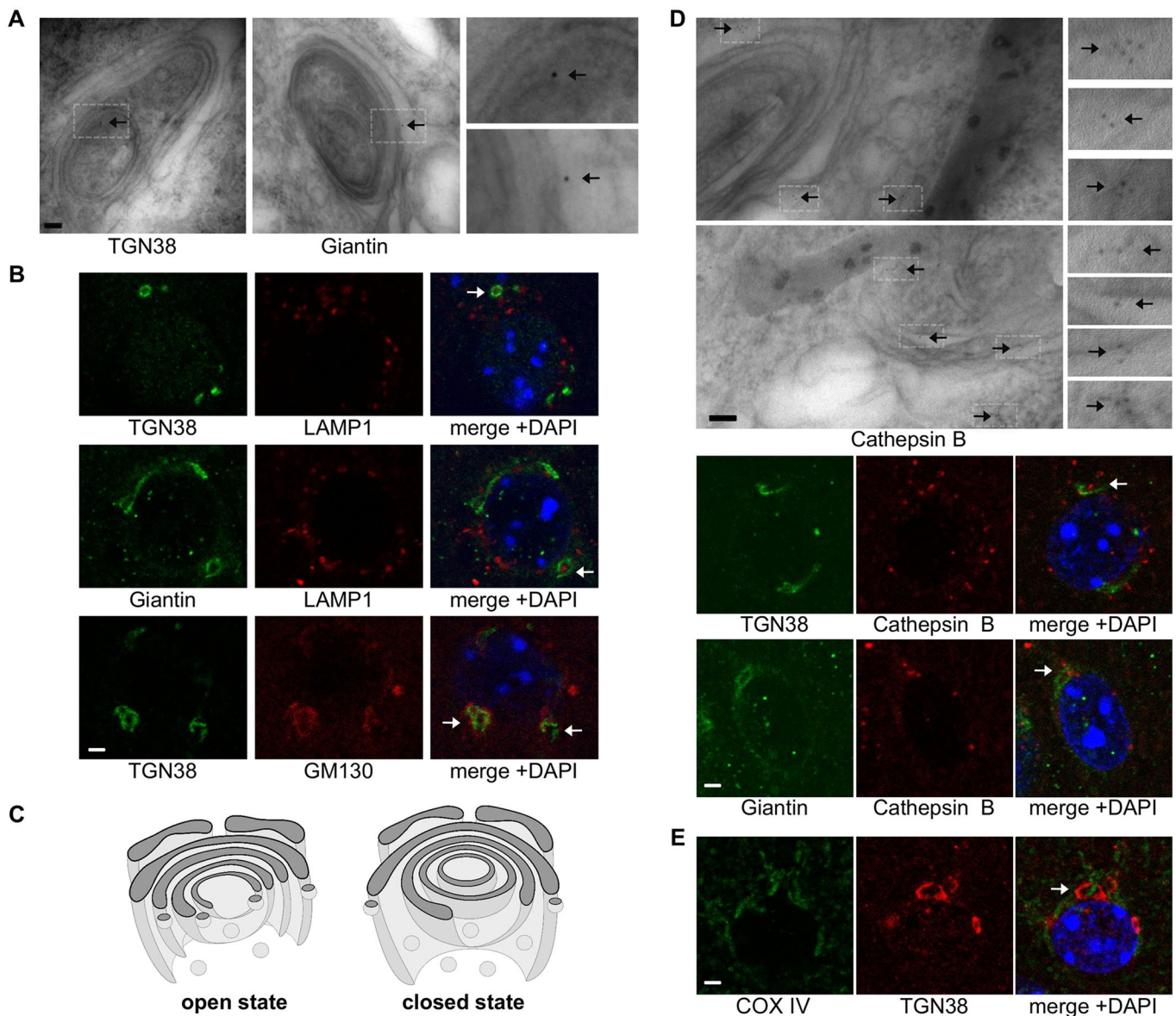
Fig. 4. Orientation of cisternae and the potential degradative nature of the engulfing Golgi. (A) Immunolabelling of 250-nm sections with anti-TGN38 and anti-giantin antibodies showed that they labelled the inner and outer layers, respectively. (B) Confocal microscopy analysis and use of these Golgi markers and GM130, a cis-Golgi marker, identified structures with dimensions compatible with the Golgi structures reported here (arrows) and confirmed the cisternae orientation identified in A. LAMP1 labelling was found close to the TGN38 and giantin labelling of these structures (upper and centre panels, orthogonal views in Fig. S1D). (C) Model of the formation of the engulfing Golgi structures. The region shown in dark grey represents a cross-section of the 3D structure. The structures develop gradually through simultaneous bending of the Golgi cisternae, which forms a cup-shaped structure of concentric double-membraned layers engulfing cytoplasmic components. The cisternae continue their bending and extension, assisted by the fusion of vesicles derived from the Golgi. Eventually, the isolation structure becomes sealed, sequestering the cytoplasmic material. (D) Immunolabelling for cathepsin B revealed the presence of this enzyme in the core structure and in Golgi-derived vesicles (two representative electron microscopy images are shown). Confocal microscopy analysis confirmed that the labelling of cathepsin B was found in the proximity of Golgi markers. (E) Confocal microscopy analysis for COX IV (mitochondrial inner membrane protein) and TGN38 corroborates the engulfment of mitochondria in the Golgi (orthogonal views in Fig. S1E). In A and D, the position of gold-particles is highlighted with arrows, and enlarged images of the areas enclosed by the dashed rectangles are shown in the panels on the right. Images in A and D are from 9-month-old male mice. Confocal images in the upper panel of B and in E are from 6-month-old male mice, and in the centre and bottom panels of B and in D images are from 2-month-old female mice. DAPI was used for nuclear staining in B,D,E. Scale bars: 100 nm (electron microscopy images in A,D); 2 µm (confocal images B,D,E).

MATERIALS AND METHODS

High-pressure freezing

Fig. S4 shows a scheme of the procedure for sample preparation. C57BL/6J mice (Jackson Laboratories) were kept as part of stable colonies in the animal facility with food and water available *ad libitum*. Experiments complied with Spanish and European legislation and Spanish National Research Council (CSIC) ethics committees on animal experimentation. Two animals of each age (2, 6 and 9 months) were processed in three different experiments. Mouse brains were dissected immediately post-mortem and 200-µm sagittal slices were obtained from the right hemisphere by using a tissue slicer (Stoelting, Co., Dublin, Ireland). Slices were promptly transferred to a device in which they were maintained under constant oxygenation (95% O_2 and 5% CO_2) in artificial cerebrospinal fluid (124 mM NaCl, 2.7 mM KCl, 1.25 mM KH_2PO_4, 10 mM glucose, 26 mM $NaHCO_3$ and 2 mM $CaCl_2$). Slices were then consecutively processed one by one. A sample punch provided

by Leica Microsystems (Wetzlar, Germany) was used to extract striatal samples from the slices after incubating them in a cryoprotectant solution (10% Ficoll) for 2 min. Samples were placed on a flat specimen carrier (0.5-mm thick, 1.5 mm in diameter, 200-µm deep, Leica Microsystems, #16706898) and high-pressure-frozen in a Leica EMPACT2 device. For a given animal, the entire processing time (from the slicing to HPF) varied from 5 min (first slice processed) to a maximum of 30 min (last slice). HPF-processed samples were maintained in liquid nitrogen until further processing.

For control purposes, samples from selected slices were processed by using conventional electron microscopy methods. The protocol included fixation with 4% paraformaldehyde and 2% glutaraldehyde, followed by post-fixation with 1% OsO_4 and 0.8% potassium ferrocyanide, incubation with 2% uranyl acetate, dehydration and embedding in epoxy resin.

Freeze-substitution, embedding and ultramicrotomy

Flat carriers containing the frozen samples were placed inside a flow-through ring (Leica Microsystems, cat. # 16707157), and this was placed in a reagent bath (Leica Microsystems, cat. # 16707154) for the substitution and embedding steps in the Leica AFS2 EM FSP system. For the freeze-substitution to methanol, the following consecutive incubations in 0.5% uranyl acetate (UrAc) were performed: overnight at −90°C, 8 h at −90°C, overnight at −90°C and 8 h at −90°C, changing to fresh solution between incubations. Temperature was then raised from −90°C to −40°C for 7 h, and then samples were incubated at −40°C for 30 h. Finally, three washes with 100% methanol were made to remove remaining UrAc.

For resin embedding, the following consecutive incubations were performed: 3:1 mixture of methanol:Lowicryl resin HM20 (Lowicryl HM20 kit, Polysciences, PA; cat. #15924) for 1 h at −40°C, 1:1 mixture for 1 h at −40°C, 1:3 mixture for 2 h at −40°C, resin for 15 min at −40°C and fresh resin overnight at −40°C. After an extra change to fresh resin, the polymerization was performed at −40°C under UV light for 48 h. The temperature was then raised from −40°C to 20°C for 4 h and then the sample was incubated at 20°C for 48 h, all under UV light. Resin capsules containing the sample were detached from the flat carriers by hot (50°C) and cold (liquid nitrogen) cycles. 250-nm-thick sections were obtained using a Leica Ultracut EM-UC6 ultramicrotome. The sections were placed on Quantifoil® S7/2-200 mesh gold (Au) grids (Quantifoil Micro Tools GmbH, Grossloebichau - Jena, Germany). We observed an average of 15 grids per animal, with four 250-nm-thick sections per grid. To check the integrity of the tissue and to identify structures of interest for further electron tomography analysis, samples were observed with a JEOL JEM-1011 100 kV transmission electron microscope.

Electron tomography

Images from 250-nm sections were obtained by using a FEI Tecnai G2 200 kV transmission electron microscope. The sections were subjected to tilt-series acquisition, where a set of images was taken by tilting the sample around a single-tilt axis in the range ±60° at an interval of 1°. The acquired images were rescaled by a four-fold binning factor to yield a pixel size at the specimen level in the range 1.56–2.33 nm. Standard electron tomography processing then followed (Fernandez, 2012), using patch-tracking-based alignment with IMOD (Kremer et al., 1996) and Weighted-BackProjection reconstruction with Tomo3D software (Agulleiro and Fernandez, 2011). The resulting tomogram was subjected to noise reduction using slight Gaussian filtering (Martinez-Sanchez et al., 2011). 3D modelling relied on automated segmentation (Martinez-Sanchez et al., 2014) followed by manual refinement of membranes unambiguously identified in *xy*-slices of the tomograms. Faint membranes perpendicular to the electron beam direction were left out of the segmentation. Manual tracing and 3D visualization was performed using Amira software (FEI Visualization Sciences Group).

Immunolabelling

Grids containing 250-nm sections were floated on top of drops and sequentially incubated with 1% periodic acid for 10 min, three times with H_2O for 3 min, 5% sodium periodate for 20 min and three times with H_2O for 3 min. Grids were then blocked with a filtered solution containing 10%

fetal bovine serum (FBS) and 0.1% Triton X-100 for 1 h. Primary antibodies – rabbit anti-giantin (PRB-114c, Covance), anti-TGN38 (NB110-40768, Novus Biologicals) and anti-LC3 (NB100-2220, Novus Biologicals), and mouse monoclonal anti-cathepsin-B (ab58802, Abcam) antibodies – were used at 1/100 dilution and incubated at 4°C overnight. An additional blocking step of 15 min was performed before the incubation at room temperature with a 1/40 dilution in 10% FBS of the secondary antibody for 45 min. A 10-nm-gold-conjugated secondary antibody [BB International EM, goat F(ab')2 anti-rabbit IgG] and a 5-nm-gold-conjugated secondary antibody [BB International EM, goat F(ab')2 anti-mouse IgG+IgM] were used. The immunolabelling of plastic sections is inefficient (58% of the analyzed structures were labelled for TGN38 and 46% for cathepsin B). The number of gold particles associated to each structure was also very low. Samples were observed by using a JEOL JEM-1011 100 kV transmission electron microscope.

Immunofluorescence and confocal microscopy

Samples were processed as described previously (Fernandez-Fernandez et al., 2011). Primary antibodies used were: rat anti-LAMP1 (1D4B, Developmental Studies Hybridoma Bank; 1/50); rabbit antibodies against TGN38 (NB110-40768 and NBP1-03495SS, Novus Biologicals; 1/200), giantin (PRB-114c, Covance; 1/1000) and LC3 (NB100-2220SS, Novus Biologicals; 1/300); goat polyclonal anti-cathepsin-B (SC-6493, Santa Cruz; 1/250); and mouse monoclonal antibodies against GM130 (610822, BD Transduction; 1/200) and CoxIV (#11967, Cell Signalling; 1/300). The secondary antibodies used were: goat anti-rat IgG conjugated to Alexa-Fluor-594, goat anti-rabbit IgG conjugated to Alexa-Fluor-488 and goat anti-mouse IgG conjugated to Alexa-Fluor-594 for Fig. 4B; donkey anti-rabbit IgG conjugated to Alexa-Fluor-488 and donkey anti-goat IgG conjugated to Alexa-Fluor-546 for Fig. 4D; goat anti-mouse IgG conjugated to Alexa-Fluor-488 and goat anti-rabbit IgG conjugated to Alexa-Fluor-594 for Fig. 4E; and goat anti-rabbit IgG conjugated to Alexa-Fluor-488 for Fig. S1C. Secondary antibodies were obtained from Life Technologies and were used at a 1/500 dilution. Nuclei were stained with DAPI (Sigma, 1/200 dilution). Images were taken on a Leica TCS SP5 confocal multispectral system. All the images are single confocal sections taken with a 63×1.4 NA objective. The optical section thickness was 0.773 µm and the pinhole was 1 AU. Single confocal sections belong to series taken with a step size of 0.7 µm.

Western blot analysis

Samples were processed as described previously (Fernandez-Fernandez et al., 2011). Membranes were incubated with a rabbit-polyclonal anti-LC3 antibody (NB100-2220SS, Novus Biologicals) at a 1/500 dilution and then with horseradish peroxidase (HRP)-conjugated anti-rabbit IgG secondary antibody (NA9340V, GE Healthcare) at a 1/1000 dilution. The peroxidase reaction was developed with Clarity™ western ECL substrate (Bio-Rad).

Supplementary information
Supplementary information available online at
http://jcs.biologists.org/lookup/doi/10.1242/jcs.188060.supplemental

References
Agulleiro, J. I. and Fernandez, J. J. (2011). Fast tomographic reconstruction on multicore computers. *Bioinformatics* **27**, 582-583.
Boland, B., Kumar, A., Lee, S., Platt, F. M., Wegiel, J., Yu, W. H. and Nixon, R. A. (2008). Autophagy induction and autophagosome clearance in neurons: relationship to autophagic pathology in Alzheimer's disease. *J. Neurosci.* **28**, 6926-6937.
Cuervo, A. M. and Macian, F. (2012). Autophagy, nutrition and immunology. *Mol. Aspects Med.* **33**, 2-13.
Fernandez, J.-J. (2012). Computational methods for electron tomography. *Micron* **43**, 1010-1030.
Fernandez-Fernandez, M. R., Ferrer, I. and Lucas, J. J. (2011). Impaired ATF6alpha processing, decreased Rheb and neuronal cell cycle re-entry in Huntington's disease. *Neurobiol. Dis.* **41**, 23-32.
Hara, T., Nakamura, K., Matsui, M., Yamamoto, A., Nakahara, Y., Suzuki-Migishima, R., Yokoyama, M., Mishima, K., Saito, I., Okano, H. et al. (2006). Suppression of basal autophagy in neural cells causes neurodegenerative disease in mice. *Nature* **441**, 885-889.
He, W. and Fernandez, J. J. (2010). Electron tomography. In: *Encyclopedia of Life Sciences (ELS)*. Chichester: John Wiley & Sons, Ltd.
Komatsu, M., Waguri, S., Chiba, T., Murata, S., Iwata, J.-i., Tanida, I., Ueno, T., Koike, M., Uchiyama, Y., Kominami, E. et al. (2006). Loss of autophagy in the central nervous system causes neurodegeneration in mice. *Nature* **441**, 880-884.
Kornfeld, S. and Mellman, I. (1989). The biogenesis of lysosomes. *Annu. Rev. Cell Biol.* **5**, 483-525.
Korogod, N., Petersen, C. C. and Knott, G. W. (2015). Ultrastructural analysis of adult mouse neocortex comparing aldehyde perfusion with cryo fixation. *eLife* **4**, e05793.
Kremer, J. R., Mastronarde, D. N. and McIntosh, J. R. (1996). Computer visualization of three-dimensional image data using IMOD. *J. Struct. Biol.* **116**, 71-76.

Luzio, J. P., Pryor, P. R. and Bright, N. A. (2007). Lysosomes: fusion and function. *Nat. Rev. Mol. Cell Biol.* **8**, 622-632.
Martinez-Sanchez, A., Garcia, I. and Fernandez, J.-J. (2011). A differential structure approach to membrane segmentation in electron tomography. *J. Struct. Biol.* **175**, 372-383.
Martinez-Sanchez, A., Garcia, I., Asano, S., Lucic, V. and Fernandez, J.-J. (2014). Robust membrane detection based on tensor voting for electron tomography. *J. Struct. Biol.* **186**, 49-61.
Mizushima, N., Yamamoto, A., Matsui, M., Yoshimori, T. and Ohsumi, Y. (2004). In vivo analysis of autophagy in response to nutrient starvation using transgenic mice expressing a fluorescent autophagosome marker. *Mol. Biol. Cell* **15**, 1101-1111.
Mizushima, N., Levine, B., Cuervo, A. M. and Klionsky, D. J. (2008). Autophagy fights disease through cellular self-digestion. *Nature* **451**, 1069-1075.
Nixon, R. A., Wegiel, J., Kumar, A., Yu, W. H., Peterhoff, C., Cataldo, A. and Cuervo, A. M. (2005). Extensive involvement of autophagy in Alzheimer disease: an immuno-electron microscopy study. *J. Neuropathol. Exp. Neurol.* **64**, 113-122.
Ohashi, Y. and Munro, S. (2010). Membrane delivery to the yeast autophagosome from the Golgi-endosomal system. *Mol. Biol. Cell* **21**, 3998-4008.
Rostaing, P., Real, E., Siksou, L., Lechaire, J.-P., Boudier, T., Boeckers, T. M., Gertler, F., Gundelfinger, E. D., Triller, A. and Marty, S. (2006). Analysis of synaptic ultrastructure without fixative using high-pressure freezing and tomography. *Eur. J. Neurosci.* **24**, 3463-3474.
Siksou, L., Varoqueaux, F., Pascual, O., Triller, A., Brose, N. and Marty, S. (2009). A common molecular basis for membrane docking and functional priming of synaptic vesicles. *Eur. J. Neurosci.* **30**, 49-56.
Studer, D., Zhao, S., Chai, X., Jonas, P., Graber, W., Nestel, S. and Frotscher, M. (2014). Capture of activity-induced ultrastructural changes at synapses by high-pressure freezing of brain tissue. *Nat. Protoc.* **9**, 1480-1495.
Traub, L. M. and Kornfeld, S. (1997). The trans-Golgi network: a late secretory sorting station. *Curr. Opin. Cell Biol.* **9**, 527-533.
van der Vaart, A. and Reggiori, F. (2010). The Golgi complex as a source for yeast autophagosomal membranes. *Autophagy* **6**, 800-801.
Young, A. R. J., Chan, E. Y. W., Hu, X. W., Köchl, R., Crawshaw, S. G., High, S., Hailey, D. W., Lippincott-Schwartz, J. and Tooze, S. A. (2006). Starvation and ULK1-dependent cycling of mammalian Atg9 between the TGN and endosomes. *J. Cell Sci.* **119**, 3888-3900.